Xu, Yang; Mao, Huachao; Liu, Cenyi; Du, Zhengyu; Yan, Weijia; Yang, Zhuoyuan; Partanen, Jouni; Chen, Yong

Hopping Light Vat Photopolymerization for Multiscale Fabrication

Published in:
Small

DOI:
10.1002/smll.202205784

Published: 15/03/2023

Document Version
Publisher's PDF, also known as Version of record

NANO · MICRO small
www.small-journal.com

Hopping Light Vat Photopolymerization for Multiscale Fabrication

*Yang Xu, Huachao Mao, Cenyi Liu, Zhengyu Du, Weijia Yan, Zhuoyuan Yang, Jouni Partanen, and Yong Chen**

3D objects with features spanning from microscale to macroscale have various applications. However, the fabrication of such objects presents challenges to additive manufacturing (AM) due to the tradeoffs among manufacturable feature resolution, maximum build area, and printing speed. This paper presents a projection-based AM process called hopping light vat photopolymerization (HL-VPP) to address this critical barrier. The key idea of HL-VPP is to synchronize linear scanning projection with a galvo mirror's rotation. The projector moves continuously at a constant speed while periodically rotating a one-axis galvo mirror to compensate for the projector's linear movement so synchronized hopping motion can be achieved. By this means, HL-VPP can simultaneously achieve large-area (over 200 mm), fast-speed (scanning speed of 13.5 mm s^{-1}), and high-resolution (10 µm pixel size) fabrication. The distinguishing characteristic of HL-VPP is that it allows for hundreds of times lower refresh rates without motion blur. Thus, HL-VPP decouples the fabrication efficiency limit imposed by the refresh rate and will enable super-fast curing in the future. This work will significantly advance VPP's use in applications that require macroscale part size with microscale features. The process has been verified by fabricating multiple multiscale objects, including microgrids and biomimetic structures.

1. Introduction

Since invented in the 1980s by Chuck Hull,[1] vat photopolymerization (VPP) has become a widely used additive manufacturing (AM, a.k.a. 3D printing) process with expanding applications in areas like rapid prototyping and manufacturing,[2,3] dentistry,[4] microfluidic chips,[5] and biomedical devices.[6,7] In principle, VPP utilizes light irradiation (laser beam scanning or mask image projection) to trigger photopolymerization and solidify liquid photocurable resin. Repeating this process layer by layer produces 3D objects. Laser spots and projection images are the two main light sources used in the VPP processes. Laser-based VPP uses a focused ultraviolet (UV) laser spot to draw a pre-programmed 2D pattern on the resin surface to form a single layer of the desired 3D object.[8–10] While the resolution could be very high with a tightly focused laser spot, the fabrication speed is unsatisfactory, especially for large solid parts, due to the nature of the scanning mechanism. Static projection-based VPP simultaneously fabricates a whole layer of a 3D object by projecting a mask image of a layer on the entire surface of liquid polymer resin.[11–19] Each pixel of an arbitrary mask image can be digitally tuned by a digital micromirror device (DMD) chip or a liquid crystal display (LCD) screen, the two most commonly used methods in VPP. Compared with the laser-based VPP process, the projection-based VPP has 10–100 times higher fabrication speed, for example, 10–100 µm s^{-1} along the building direction,

Y. Xu, Y. Chen
Center for Advanced Manufacturing
University of Southern California
Los Angeles, CA 90007, USA
E-mail: yongchen@usc.edu

Y. Xu, C. Liu, W. Yan, Z. Yang, Y. Chen
Department of Aerospace and Mechanical Engineering
University of Southern California
Los Angeles, CA 90089, USA

The ORCID identification number(s) for the author(s) of this article can be found under https://doi.org/10.1002/smll.202205784.

DOI: 10.1002/smll.202205784

H. Mao
School of Engineering Technology
Purdue University
West Lafayette, IN 47907, USA

Z. Du
Mork Family Department of Chemical Engineering and Materials Science
University of Southern California
Los Angeles, CA 90089, USA

Y. Chen
Daniel J. Epstein Department of Industrial and Systems Engineering
University of Southern California
Los Angeles, CA 90089, USA

J. Partanen
Department of Mechanical Engineering
Aalto University
Puumiehenkuja 5, Espoo 02150, Finland

when printing macroscale objects.[11–14] However, the limited quantity of pixels in a DMD chip or an LCD screen (e.g., 1920 × 1080) constrains the build area size to maintain an acceptable feature resolution for static projection-based VPP (e.g., mesoscale VPP[11–14] and microscale VPP[15–19]). That is, the printing resolution will decrease with the increase of printing area because the mask image pixel size scales up simultaneously. This dilemma of the part-to-pixel (PTP) size ratio hinders static projection-based VPP from fabricating macroscale (decimeter scale) objects with delicate microscale (micrometer scale) features. Such multiscale structures have broad applications, for example, the human lung structure spanning multiple size scales (**Figure 1**a).[20,21]

1.1. Related Works

Intensive research works have been done to improve VPP's performance regarding fabrication speed,[11–13,22–25] part size,[12–14] and feature resolution.[15–19] However, most methods have to optimize only two of the three core manufacturing metrics (speed, resolution, and size) at most by sacrificing the other. It has been challenging to optimize the three aspects simultaneously. How to achieve a large PTP ratio (e.g., efficiently fabricating millions of microscale features over a macroscale surface) without increasing production time and hardware costs is still an open question. We conducted a comprehensive literature study and classified the related works contributing to increasing PTP ratios into three categories.

The first category of the strategies is to combine $n \times m$ projects to cover an increased projection area or to combine two light sources with fabrication capabilities at different scales. For example, a projector[26,27] or a laser with a large spot size[28,29] (e.g., 800 μm) is utilized to fabricate the interior of each layer. A laser with a tiny spot size (e.g., 30 μm) is used to cure the contours and microscale features. However, this kind of method will either result in significantly increased cost or a slower printing speed due to the nature of the scanning mechanism. In addition, a limited printable area can be achieved due to the fixed light sources.

The second category of methods[30,31] utilizes the pixel blending principle to improve the resolution without sacrificing production efficiency. Unlike static projection, the fabrication of each layer is accomplished by projecting n^2 mask images with subpixel size-shifting (p/n, p is the nominal pixel size of the projector) between each projection. The combination of n^2 mask image projections delivers the same energy level to cure photopolymer as a single static mask image projection but features a higher resolution ($p_s = p/n$, p_s is the nominal pixel size in the pixel shifting method). The challenge of this method lies in the computation of large amounts of mask images and the fundamental limitation on the fabrication accuracy due to pixel blending errors.

The third type is to split a projection area into many sections such that multiple projections at various places can be used to complete one-layer fabrication. A straightforward method to break the print area limit is the well-known step-and-repeat process.[32,33] A projector or the build platform moves and stops at a specified position by motorized stages and then makes a projection. Each subarea is printed using a consistently higher resolution than static projection (see Figure 1b,c for comparison). Hence macro objects can be fabricated without losing detailed features. However, the fabrication time will dramatically increase when manufacturing large objects due to the frequent small displacement and on-off switch of the projector. To eliminate the extra transition time in the step-and-repeat method,[32,33] researchers proposed a moving light strategy,[35–41] in which the projector moves continuously while projecting mask images simultaneously (Figure 1d). The projector needs to refresh the mask image with every movement of a one-pixel distance. Otherwise, the motion blur effect will lead to incorrect curing (see Figure 1d,c for comparison). Although promising for its fabrication speed, the high image refresh rate required for the projector requires a customized graphics controller and limits the achievable moving speed. That is, the required projector frame rate should be at least $F = v_s/(K_m p)$, where v_s is the mask image scanning speed, namely the projector moving speed, and p is the pixel size. $K_m = D_m/p$ denotes relative marching steps, the ratio of image marching distance D_m to pixel size p. The factor K_m evaluates mask image switching frequency from the spatial perspective. For the moving light strategy, $K_m = 1$. Given the same layer thickness, a larger v_s is always desired for fabrication efficiency. Suppose the mask image scanning speed is 100 mm s^{-1} and the pixel size is 10 μm which is common in microscale VPP. The projector refresh rate needs to be above 10 kHz, which is incredibly high and beyond the capability of most commercially available graphics cards. This requirement also challenges most commercially available projectors and is only possible for costly customized projectors and graphics cards with significantly increased buffer volume and transfer rate. For a 1080P projector (resolution: 1920 × 1080), the transfer rate would be at least 2.592 Gbit s^{-1}, and the slice data for an entire part can run into several terabytes easily.[40] Another method to expand the build area is to use two-axes galvo mirrors to rapidly move the projection image's position in a build area,[34] similar to conventional laser-based VPP. The method is fast (3.33 mm^3 s^{-1}) with high resolution (5 μm pixel size); however, a key bottleneck of the method is it requires a customized f-theta lens to compensate for the varying focal length so the reflected 2D images can be focused on the building plane. The limited field of view of the f-theta lens constrains the achievable printing area (up to 100 × 100 mm^2). Initially designed for a small laser spot (≈50 μm), the *f*-theta lens may have limited ability to compensate for the focal length variance of a 2D image in centimeters.

1.2. Our Approach and Contributions

The research mentioned above is inspiring that can improve static VPP's performance. But the research gap still exists in solving the tradeoff among maximal part size, resolution, and printing speed. This paper presents a highly efficient method called hopping light (HL) to cover a large build area using only off-the-shelf components. The key idea of HL is to anchor the moving image using a galvo mirror's reverse rotation in each cycle and then to start a new cycle utilizing the galvo mirror's fast-rotating capability (Figure 1e). As shown in the laser-based

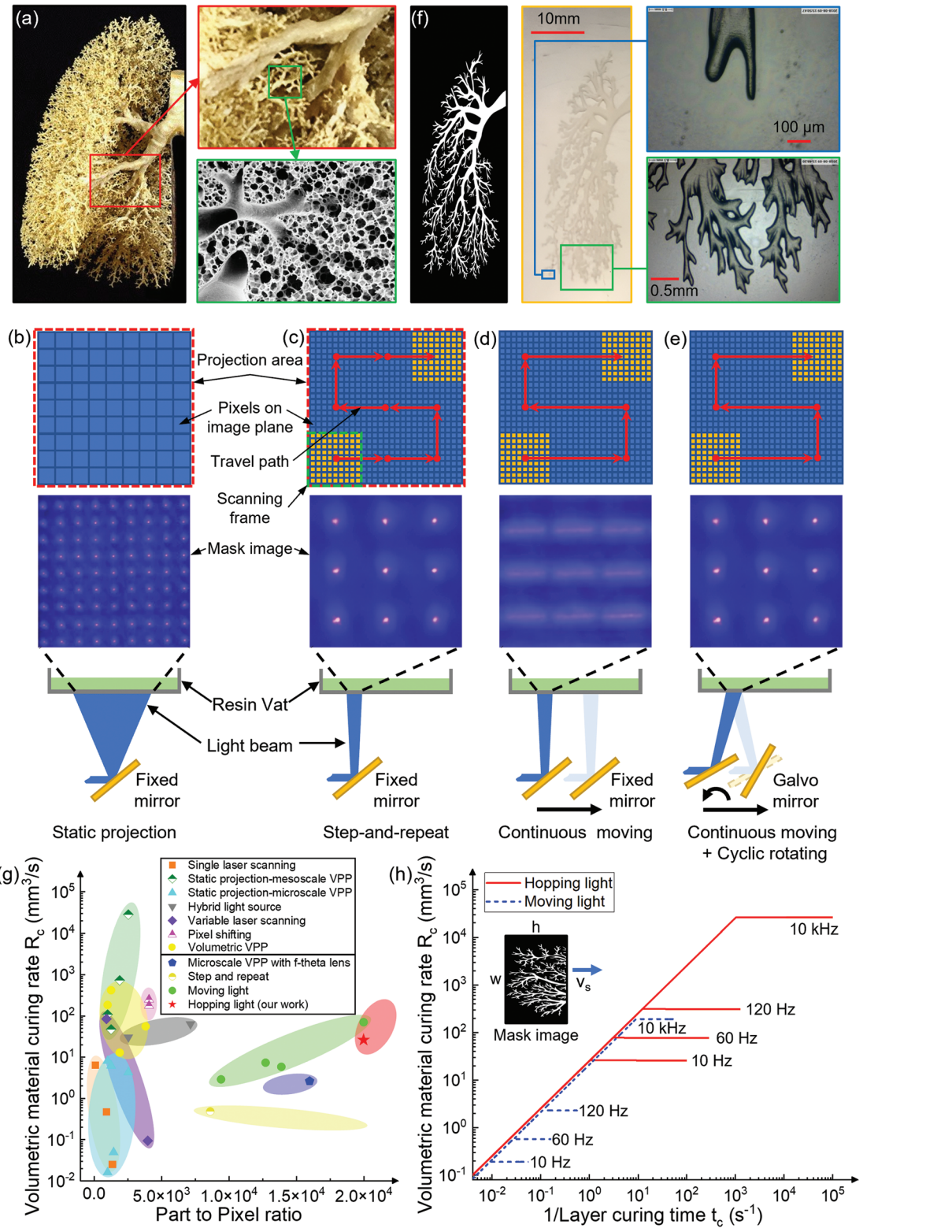

Figure 1. Introduction of different VPP processes and related applications. a) Human lung structure model. Reproduced with permission.[20] Copyright 2017, Springer. Reproduced with permission.[21] Copyright 2006, AIMS, LLP. b) Schematic of mesoscale static projection-based VPP. c) Schematic of the step-and-repeat method. d) Schematic of the moving light method and the motion blur issue when the projector refresh rate is not sufficiently high. e) Schematic of the hopping light method. f) One layered mask image of the human lung model and the corresponding printing result using HL-VPP. Reproduced with permission.[42] Copyright 2017, Dreamstime. g) Summary of various VPP processes in the literature regarding printing efficiency R_c and PTP ratio. h) Relationship between the volumetric material curing rate R_c and the curing time t_c given the same layer thickness 100 μm for the moving light and hopping light methods.

VPP, a galvo mirror can have a fast response rate (in kHz), while the much heavier projector can move continuously at a desired scanning speed v_s. First, the galvo mirror to reflect the mask image onto the building plane rotates continuously to compensate for the projector movement, so the projection image remains static during each cycle (e.g., 0.1 s used in our tests). Then, at the end of each cycle, the galvo mirror rotates sharply back to its initial position within microseconds, suddenly leading to the curing region hopping to the next section. Meanwhile, the projector refreshes the mask image. Hence the projector only needs to refresh the mask image once during each cycle, instead of after moving a single pixel size in the moving light method, dramatically diminishing the projector's frame rate requirement (K_m = 135, F = 10 Hz in our case, see Section 2 for details). The motion blur issue has been avoided by the reverse movement of the scanning mirror (see Figure 1e,d for comparison). From the top view of the resin vat, the projected image keeps static within each cycle of the curing process and swiftly hops to the next section in sequence (Movie S1, Supporting Information). The developed hopping light vat photopolymerization (HL-VPP) can produce multiscale structures spanning from microscale to decimeter scale or even larger. Our approach can maintain high resolution (10 μm per pixel) when printing large parts (200 mm). Figure 1f shows one layer of mask image of a human lung model[42] and the corresponding fabrication result via HL-VPP. The image strip was printed during one movement with a scanning speed of 13.5 mm s^{-1}.

Figure 1g and Table S1(Supporting Information) summarize various VPP processes in the literature regarding fabrication efficiency and PTP ratio. In addition to the demonstrated results from the literatures, Figure 1g also indicates the potential ranges of each method by using ellipses based on the nature of the technique. For example, both the step-and-repeat process[32] and the moving light method can achieve a large build area by using a linear stage with an increased travel range; hence a range of PTP ratios can be theoretically achieved that are shown in the figure. From Figure 1g, the single laser scanning method features a lower fabrication speed similar to static microscale projection-based VPP. Static mesoscale projection-based VPP can achieve an extremely high material curing rate (more than 20 000 mm^3 s^{-1}) but is limited in the PTP ratio (defined by the DMD or LCD resolution). The fabrication speed will inevitably decrease for other processes aiming at a large PTP ratio. Only the VPP processes involving moving light sources can achieve an arbitrarily large PTP ratio. The fabrication efficiency of the step-and-repeat method is generally lower than the moving light approach due to the additional time in projector transition, as shown in Figure 1g and discussed in Section 1.1. Moving light saves fabrication time by synchronizing projector scanning and mask image refreshing. However, a faster curing rate R_c requires a higher refresh rate F. This relationship can be easily seen in Figure 1h. Given a layer thickness l (0.1 mm in Figure. 1h), a shorter curing time t_c allows for a faster scanning speed and thus leads to a higher curing rate as $R_c = l \times w \times v_s = lwh/t_c$, where w and h are the mask image width and height respectively and the scanning direction is along h. The curing rate will finally reach an upper bound defined by the refresh rate because $R_c = l \times w \times v_s = lwK_m pF = lwpF$, as discussed in Section 1.1. In comparison, our HL-VPP can reduce the projector refresh rate requirement by one thousand times (10 kHz vs 10 Hz) because K_m = 135 in our case (see Section 2 for details). Our method opens up the possibility of achieving a much higher curing rate for future multiscale VPP processes. The contributions of this work are summarized here:

1. The developed HL-VPP dramatically reduces the required frame rate of the light engine used in moving light VPP to the range of commercial graphics cards and projectors (within 30 frames per second). Hence all the current commercial projectors and graphics cards can be used in HL-VPP to handle the task of mask video projection easily;
2. The HL-VPP shows high fabrication efficiency since its printing process has no waste of time during the projector's linear movement;
3. The HL-VPP method has no motion blur issue, even for a high-speed linear movement of the projector;
4. A large build area with fine features can now be achieved simultaneously within each layer, rendering our process a high PTP ratio (over 20 000).

2. Results and Discussion

2.1. HL-VPP Process Design

To realize the proposed process, a HL-VPP prototype, as shown in **Figure 2**a and Figure S1 (Supporting Information), was designed and constructed. The setup has two additional motorized linear stages (a *XY* stage) and a galvo mirror, compared with the static bottom-up-projection-based VPP. The whole optical module is mounted on the *XY* stage. The *X* stage moves the optical module continuously at a constant scanning speed v_s to cover one image strip, and the *Y* stage moves the optical module on the *Y* axis after one image strip finishes.

A fish CAD model[43] (Figure 2b) illustrates the printing process in detail. The input 3D model is first sliced into a sequence of 2D layers (Figure 2c) for a given layer thickness (e.g., 0.1 mm). Each layer (one layer is shown in Figure 2e) is further divided into an array of overlapped sections based on the image marching distance D_m (determined by v_s, e.g., 1/2 of image height shown in Figure 2e). Each section ($w \times h$ rectangle marked in purple) corresponds to a mask image and will be cured one by one. The scanning path of the *X* stage is from A_1 to D_2. The segments A_1A_2 and D_1D_2 are for acceleration and deceleration of the linear stage, respectively. The uniform motion phase starts before point A_2 and ends after point D_1. During the uniform motion A_2D_1, the DLP projector projects mask images onto the resin surface to cover one section after another (e.g., mask images marked by red and green dash lines in Figure 2e). For each section, namely each cycle of projecting a mask image, the galvo mirror conducts complementary reverse rotation periodically to cancel out the projector's movement in the *X* axis (see states I to III in Figure 2f,g). Thus, the mask image is anchored to the corresponding curing section (Figure 2g), and the motion blur effect in the continuous projector motion is corrected. By the end of each curing section, the galvo mirror swiftly jumps back to the initial position so

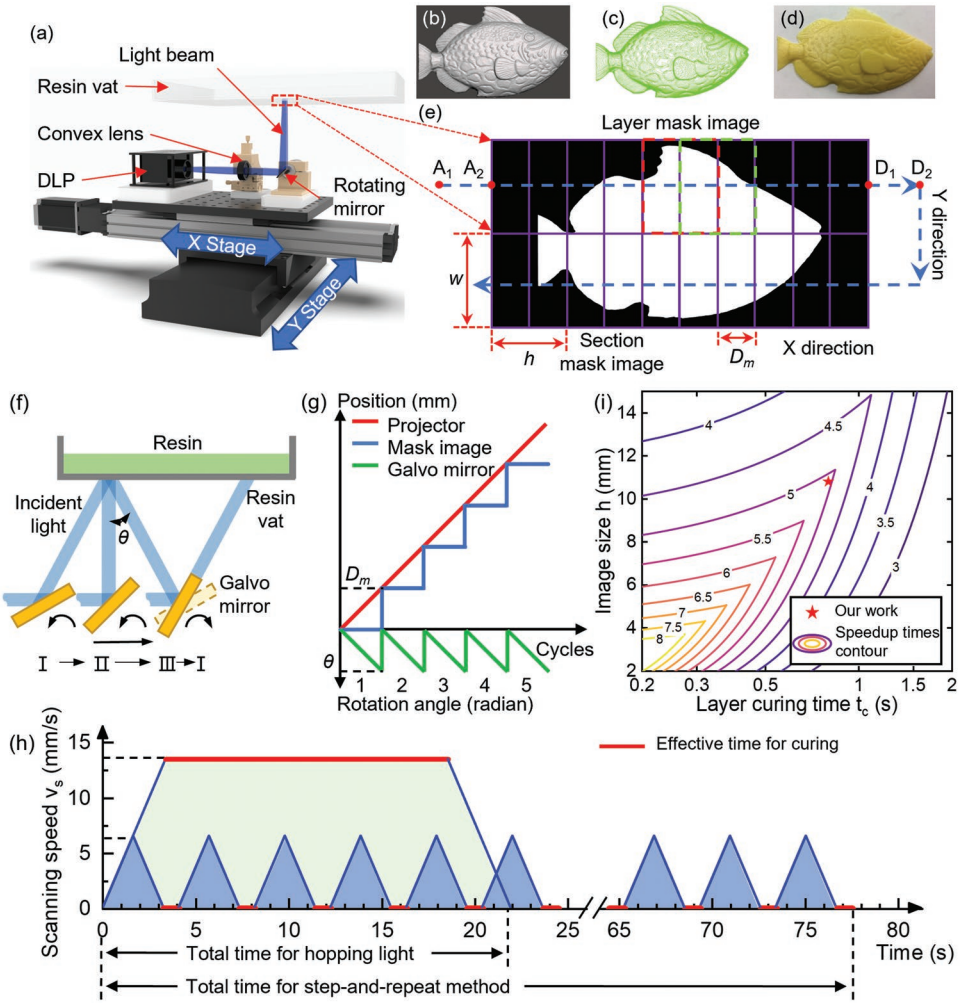

Figure 2. Principle of the HL-VPP process. a) Detailed structure of the HL-VPP prototype. b) A fish CAD model is used to illustrate the HL-VPP process. Reproduced under terms of the CC-BY license.[43] Copyright 2013, Paul Moews, published by Thingiverse. c) Contours of a set of 2D layers generated from the fish CAD model. d) 3D Printing result using HL-VPP. e) One layer mask image used to describe the HL-VPP process in detail. f) Galvo mirror's motion in one cycle. g) Illustration of the position relationship among the projector, galvo mirror, and image projection in each cycle. h) Time consumption of HL-VPP and the step-and-repeat process when fabricating the same area with the same process parameters. Red lines indicate the effective time for material curing, while blue lines represent time wasted in projector transition. i) Printing speedup of HL-VPP over step-and-repeat for different image sizes and curing times.

that the projection area hops to the next section (see state III to I in Figure 2f,g), and the DLP projects a refreshed mask image planned by the HL-VPP software system. Note the process from state III back to state I takes less than 1 ms. After the exposure of one image strip, the *Y* stage shifts the curing region perpendicularly to the next row (Figure 2e). When all the rows are covered, a *Z* linear stage moves up and down the build platform to separate the fabricated layer from the resin vat and refills fresh resin based on a given layer thickness. The layered-based process is repeated until all the layers are completed. The fabricated 3D object will be removed from the build platform and post-processed. Figure 2d shows the fabrication result using the HL-VPP process.

Figure 2h compares the velocity profiles of the proposed HL-VPP and the step-and-repeat process when fabricating the same build area (19.2 mm × 205.2 mm) with the same process parameters (one mask image size $w \times h = 19.2$ mm × 10.8 mm, acceleration rate $a_m = 4$ mm s^{-2}, maximal scanning speed $v_s = 13.5$ mm s^{-1}). By incorporating the galvo mirror, the proposed HL-VPP process can maintain a constant scanning speed to cover the printing area more efficiently than the discrete step-and-repeat process, which must frequently halt the motion system for static image projection. In addition, the projection system in the step-and-repeat process only cures the resin when the projector completely stops (when the velocity is zero, see red lines in Figure 2h). The rest of the time is wasted on the translational movement without material fabrication (see blue lines in Figure 2h). Such time inefficiency becomes more severe with reduced mask image size or faster curing time; both are desired for a higher pixel resolution and a quicker building speed. When the distance between two adjacent sections gets shorter for a small mask image, the linear stage will

not be able to accelerate to the maximal scanning speed in such quick discrete motions.

We derived the fabrication time of the same projection area $w \times h$ (mask image size) for the HL-VPP and step-and-repeat methods to quantify the speedup effect.[32,33] For HL-VPP, the fabrication time is max (t_c, h/v_s), that is, either the layer curing time t_c or the motion time of moving h at a constant scanning speed v_s, whichever is larger. For the step-and-repeat method, the corresponding fabrication time is the curing time plus the extra transition time, which has two scenarios. If the linear stage can achieve the maximal scanning speed v_s with the maximal acceleration a_m during the short translation movement, that is $a_m h > v_s^2$, the extra transition time is $h/v_s + v_s/a_m$. Otherwise, the transition time is $2\sqrt{h/a_m}$. Then the total fabrication time for the step-and-repeat method is $t_c + (h/v_s + v_s/a_m) \times (a_m h > v_s^2) + 2\sqrt{h/a_m} \times (a_m h \le v_s^2)$. Hence, the speedup ratio of HL-VPP to the step-and-repeat process is

$$\text{Speedup} = \frac{t_c + (h/v_s + v_s/a_m) \times (a_m h > v_s^2) + 2\sqrt{h/a_m} \times (a_m h \le v_s^2)}{\max(t_c, h/v_s)} \quad (1)$$

Figure 2i shows the contours of speedup Equation 1 concerning different image sizes and layer curing times, where v_s = 13.5 mm s^{-1} and a_m = 4 mm s^{-2}. The HL-VPP prototype reached 5.1 times faster with the mask image height h = 10.8 mm and the curing time t_c = 0.8 s.

2.2. Tilted Image Error Analysis and Parameter Study

When using the galvo mirror to compensate for the mask image motion, the rotating mirror tilts the image in HL-VPP, potentially changing the image size and defocusing the projection image on the building plane. This section analyzes the effect of the mask image tilting behavior, including image size and defocus errors. Accordingly, the proper focal length L and the corresponding image marching distance D_m are presented, which can guide the HL-VPP's hardware configuration and software settings.

2.2.1. Image Size Change

Tilting mask images may increase the projection size on the building surface, as illustrated in **Figure 3**a. When the projector marches a small distance D_m, the galvo mirror rotates a small angle, so the projected image's center is maintained in the same place. We define D_m as the image marching distance in a cycle. During the periodic motion, the mask image is horizontally focused only at the middle position with the central distance to the galvo mirror as L. After moving a small distance, the projection image size h defined on the tilted image plane is distorted on the horizontal image plane (shown in Figure 3a—bold lines for the two planes).

The amount of image size change Δ_s depends on the magnitude of the tilting angle θ. Assume the tilting angle θ is a

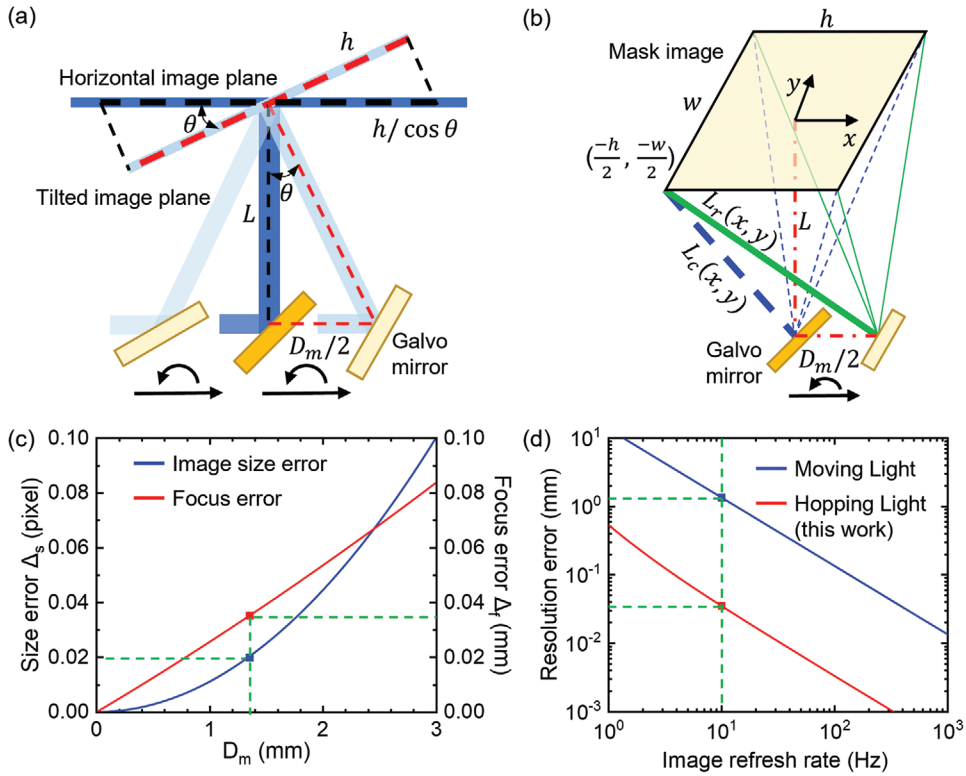

Figure 3. Error analysis on the HL-VPP process. a) Schematic illustration of image size change in each cycle of the HL-VPP process. b) Schematic illustration of light path change in each cycle of the HL-VPP. c) Image size and focus errors of HL-VPP with different image marching distances. d) Resolution error comparison between the HL-VPP and Moving Light processes for different image refresh rates.

minimal value (about 0.35° in our implementation). Then the original image height h is increased to $h/\cos\theta$. The image height is changed by

$$\Delta_s = \frac{h}{\cos\theta} - h \approx \frac{h}{8}\left(\frac{D_m}{L}\right)^2 \tag{2}$$

Equation 2 characterizes the image size change. Figure 3c (blue line) and Equation 2 suggest that the image size error will be reduced as D_m decreases. In our prototype system, h = 10.8 mm, L = 110 mm, and D_m = 1.35 mm, the corresponding tilting angle θ is arctan $(D_m/2L) \approx 0.35°$, the size change is only 0.2 µm (or 0.02 pixels—see the blue dot in Figure 3c), which is negligible.

2.2.2. Image Focus Error

The rotating mirror will also change the length of the light path, which may affect the focus of the projection image. In each cycle, the light path length varies during the optical module's movement. The well-focused image with the shortest light path is achieved in the central position of each cycle, as shown in Figure 3b. For a pixel (x, y) in the mask image, the light path length in the well-focused state is denoted as $L_c(x, y)$. Assume the projected image size and location are not changed within one cycle (this assumption is valid as the image size is negligibly changed. See Section 2.2.1 for details.). The light path length changes to $L_r(x, y)$ when the optical system moves to the rightmost point, as shown in Figure 3b (bold lines L_r and L_c). The maximal variation in the light path during each cycle locates in the left corner of the mask image and can be computed as

$$\begin{aligned}\Delta_f &= L_r\left(\frac{-h}{2},\frac{-w}{2}\right) - L_c\left(\frac{-h}{2},\frac{-w}{2}\right)\\ &= \sqrt{\left(\frac{-w}{2}\right)^2 + \left(\frac{-h}{2} - \frac{D_m}{2}\right)^2 + L^2} - \sqrt{\left(\frac{-w}{2}\right)^2 + \left(\frac{-h}{2}\right)^2 + L^2}\\ &\approx \frac{D_m\left(D_m + 2h\right)}{8L}\end{aligned} \tag{3}$$

where L is the distance between the galvo mirror and the image plane, w and h are image width and height, respectively. Equation 3 and Figure 3c (red line) indicate that the focus error Δ_f decreases as D_m decreases. According to lens optics, the allowable depth of focus (DOF) Δ_{df} can be estimated as[44]

$$\Delta_{df} = 2Nc\frac{\upsilon}{f} = 2c\frac{\upsilon}{D} \tag{4}$$

where c is the circle of confusion, N is the lens f-number, υ is the image distance, f is the lens focal length, and D is the lens diameter. Plug the setting of our prototype—D = 25.4 mm, $\upsilon = L$ = 110 mm, and c = 0.011 mm into Equation 4. The computed DOF Δ_{df} = 0.095 mm. To avoid defocus, we could reduce D_m so the focus variation should be within half of the DOF:

$$\Delta_f < \frac{\Delta_{df}}{2} \tag{5}$$

which yields the critical image marching distance:

$$D_m < \frac{\sqrt{8\Delta L + h^2} - h}{2} \approx 1.675\ \text{mm} \tag{6}$$

Equation 6 ensures that the defocus due to image tilting does not affect the printing resolution if the image marching distance is smaller than this critical value. In our case, the mask image size is $w \times h = 19.2 \times 10.8\ \text{mm}^2$ with each pixel size p as 10 µm. We set D_m to 1.35 mm, which equals 135 pixels, 1/8 of the image height. The corresponding focus error is about 0.035 mm, smaller than the threshold $\Delta_{df}/2$ = 0.0475 mm, as shown in Figure 3c (red dot).

As the layer curing time t_c = 800 ms, the scanning speed $v_s = h/t_c$ = 13.5 mm s^{-1}. The relative marching steps $K_m = D_m/p$ = 135, meaning the required projector refresh rate in our case $F = v_s/(K_m p)$ = 10 Hz is 135 times lower than the moving light method[35–41] to achieve the same pixel-level resolution, or the maximal scanning speed v_s is 135 times higher if the same projector refresh rate is used.

We also quantitatively compare the resolution performance of our method with the moving light methods,[35–41] given the same image height h, image refresh rate F, and curing time t_c. The resolution error E_r of the moving light methods without image tilting[35–41] is quantified as the distance a pixel travels within an image refresh:

$$E_r = \frac{h}{Ft_c} \tag{7}$$

The resolution error E_r of our method is quantified as the focus error using Equation 3:

$$E_r = \frac{\frac{h}{Ft_c}\left(\frac{h}{Ft_c} + 2h\right)}{8L} \tag{8}$$

where h = 10.8 mm, t_c = 0.8 s, L = 110 mm.

Figure 3d compares our method's resolution error introduced by image tilting (Equation 7) and that of the moving light process caused by image motion blur (Equation 8) regarding different refresh rates F. Our approach has a much lower resolution error under the same condition.

In the HL-VPP process, an appropriate image marching distance D_m is critical to address the defocus and image size error issues. Based on the analysis of the tilted image used in our projection system, D_m is only a small fraction of the image size. This strategy of using a small image marching distance significantly diminishes the defocus effect without a decrease in scanning speed and the demanding requirement of image refresh rate.

2.3. Computer Vision-Assisted Calibration

The proposed HL-VPP relies on the synchronization among the translational movement of the X-axis linear stage, the galvo

mirror scanning, and the mask image projection. Calibrations are essential to guarantee the accuracy and performance of the HL-VPP experimental setup.

The calibration system was configured as shown in **Figure 4**a. A digital microscope was mounted on top to capture the projected image[45] focused on the resin vat surface. We aim to ensure the HL-VPP's image projection keeps static in this microscope image space during the composite motion in each cycle. The static mask image indicates the system is well-synchronized, and no motion blur exists in the photopolymerization process.

Both actuators—the linear stage and the galvo mirror can lead to the position change of the projected images. We captured the projected images before and after the individual movement of each actuator using the digital microscope and compared them in the microscope image space. For example, Figure 4b shows the microscope-captured images (enclosed by red and cyan rectangles) before and after the *X*-axis linear stage moves by 1 mm. We leveraged the computer vision toolbox in MATLAB to compute the displacement between the two images in the microscope image space.[46] The corresponding algorithm is given in Table S2 (Supporting Information). The algorithm detects and matches the features between the two images and then generates a transformation matrix. As shown in Equation 9, the output matrix T indicates the geometric transformation between the two images.

$$T = \begin{bmatrix} s*\cos(\alpha) & -s*\sin(\alpha) & 0 \\ s*\sin(\alpha) & s*\cos(\alpha) & 0 \\ t_x & t_y & 1 \end{bmatrix} \tag{9}$$

where s is the scale, α is the rotation angle, t_x and t_y are the translations along the X and Y axes, respectively. In all our tests, the scale s was between 1.0 and 1.0005, which verified that the image size change was negligible, less than $0.0005 \times 1080 = 0.54$ pixels. In our application, since the image tilting angle is small, as analyzed in the above section, the captured images in the microscope image space involve translations only. Besides, the whole projection module will continuously move along the *X*-axis during projection. Hence, we only utilized the t_x value in the transformation matrix to calibrate the system. Figure 4b (enclosed by a yellow rectangle) shows the comparison result of moving the *X* stage by 1 mm. The estimated translation in the microscope image space is t_x = 122.35 pixels. Similarly, Figure 4c shows the captured images before and after the galvo mirror rotates 0.2° and the corresponding comparison result. The estimated image translation in the microscope image space is t_x = –94.31 pixels. Therefore, the velocity ratio of the galvo mirror rotation to the linear stage translation r_v is $\frac{122.35\,\text{pixels}/1\,\text{mm}}{-94.31\,\text{pixels}/0.2^\circ} = -0.2595^\circ/\text{mm}$. Only the well-calibrated velocity ratio can correct the motion blur and achieve static exposure in each cycle of HL-VPP. To verify the velocity ratio r_v derived from previous measurements, we made the *X*-axis stage move by 1.35 mm and the galvo mirror rotate by 0.35°, then checked the projected images before and after the composite motion. Figure 4d depicts the two projected images and matching results. Since the movement of the two actuators conforms to r_v, the matched feature pairs perfectly overlapped, as shown in Figure 4d (enclosed by a green rectangle and the magnified portion), which proves that the image projection maintains static during the composite motion.

Lastly, the projection image's physical size was also computed based on the microscope image space. We created two similar mask images by shifting the first one by 50 pixels along the *X*-axis (see images enclosed by red and cyan rectangles in Figure 4e). The microscope captured the two image projections respectively. The measurement results showed t_x = 61.49 pixels in the microscope image space. Referring to the calibration result for the *X* stage, we computed the physical pixel size in image projection as $\frac{61.49\,\text{pixels}/50\,\text{pixels}}{122.35\,\text{pixels}/1\,\text{mm}} \approx 10\,\mu\text{m pixel}^{-1}$. With the calibrated image size, the projection system refreshes the image precisely after the linear stage moves one image marching distance. The calibrated image size also ensures the bonding area between successive image scanning (see the overlapped area of green and red rectangles in Figure 4f and details in Figure 4g) is well stitched in the *Y* direction. Figure 4h,i compares the stitch quality before and after calibration. Misalignment between successive image scanning was found in the printed part (103.2 µm in Figure 4h) before and resolved after calibration (Figure 4i).

2.4. Microscale Structures over Macroscale Area

To verify the performance of HL-VPP, we fabricated microgrids (100 µm thickness, 300 µm spacing, and 300 µm height) and macroscale features "FIGHT ON! USC TROJANS" on the top over a 200 mm long surface, as shown in **Figure 5**a,b (Top view: Figure 5a,b Top; Side view: Figure 5b Bottom). We measured the cross-sectional dimensions of the printed microgrids using a microscope. The statistical results are give n in Figure 5c and Table S3 (Supporting Information), showing high accuracy and precision. The average dimensional error in the XY plane is within 6 µm, less than 1 pixel (10 µm). The standard deviation is also less than 10 µm. We also compared the fabrication time of HL-VPP with the step-and-repeat method, as shown in Figure 5d and Table S4 (Supporting Information). The time saving of the part shown in Figure 5a ($200 \times 60 \times 4.3$ mm^3) reaches 75% with HL-VPP.

HL-VPP can benefit 3D printing bioinspired surfaces and structures for various applications.[19,47–49] Compared with traditional static microscale VPP, which can only fabricate parts less than 15×15 mm^2, HL-VPP can achieve the same fine structures with a much larger printing size, opening opportunities for more applications. Figure 5e shows a large piece of cactus-like pillar arrays fabricated by HL-VPP (Top view). Each pillar is a 1 mm high cone with a bottom diameter of 300 µm and a tip diameter of 50 µm (Figure 5f, side view). The pitch between pillars is 600 µm. We measured the diameters of the printed cones' top and bottom layers. Figure 5g and Table S5 (Supporting Information) show the measurement results. The average size error is within 5 µm. The standard deviation is less than 10 µm. The fabrication result shows good accuracy and reliability. The well-stacked multiple layers (50 layers) also indicate that HL-VPP can maintain static projection in each cycle, having the same performance as the static projection-based

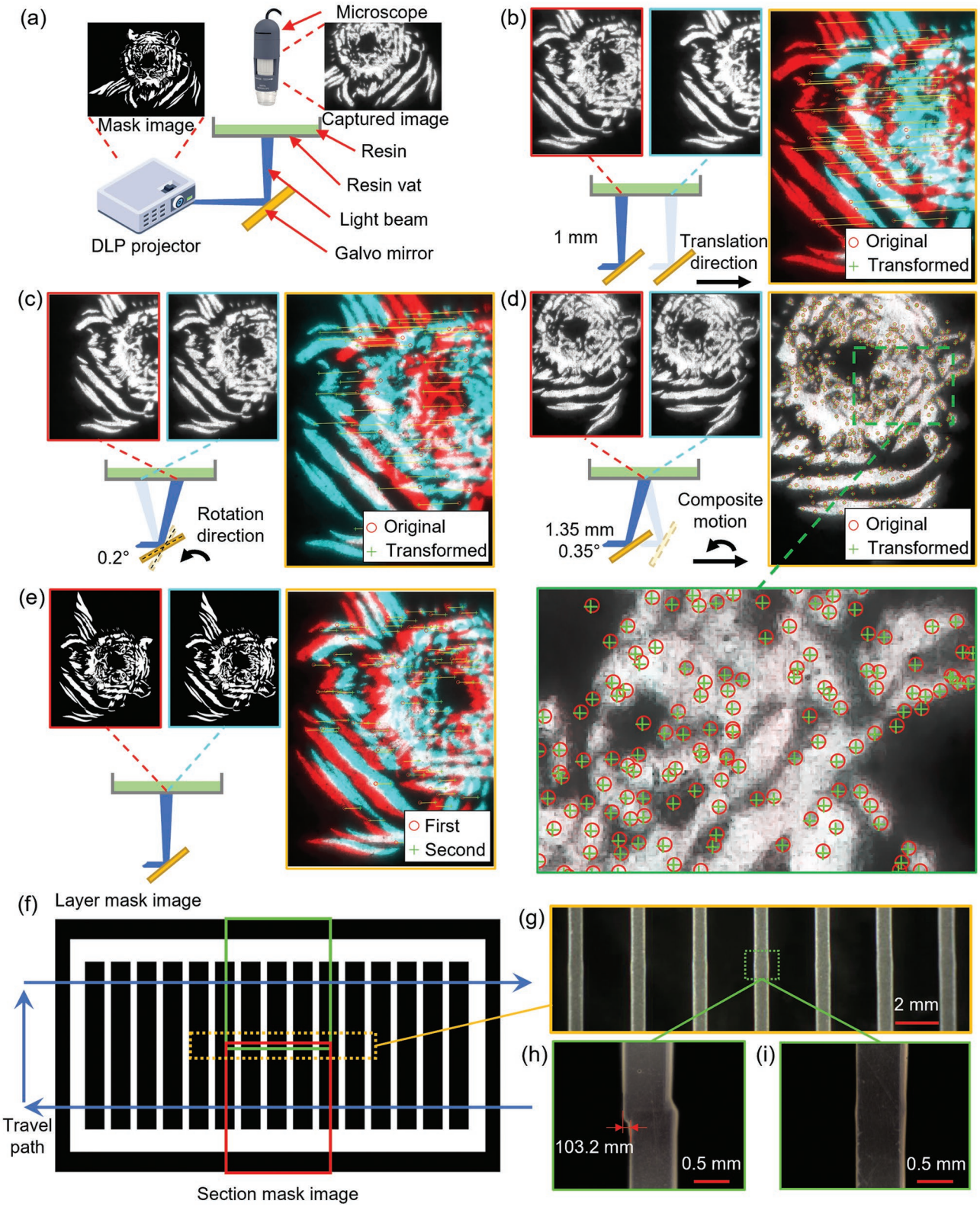

Figure 4. Computer vision-assisted calibration of the HL-VPP system. a) Schematic illustration of the HL-VPP calibration system. The handheld digital microscope was removed when printing. Reproduced with permission.[45] Copyright 2009, iStockphoto LP. b) Calibration process for the *X*-axis linear stage. c) Calibration process for the galvo mirror. d) Verification of the velocity ratio derived from the *X* stage and galvo mirror calibrations. e) Calibration of the physical mask image size. f) Calibration process for image alignment. g) Details of the part bonding area. h,i) A comparison of the part bonding area before and after calibration.

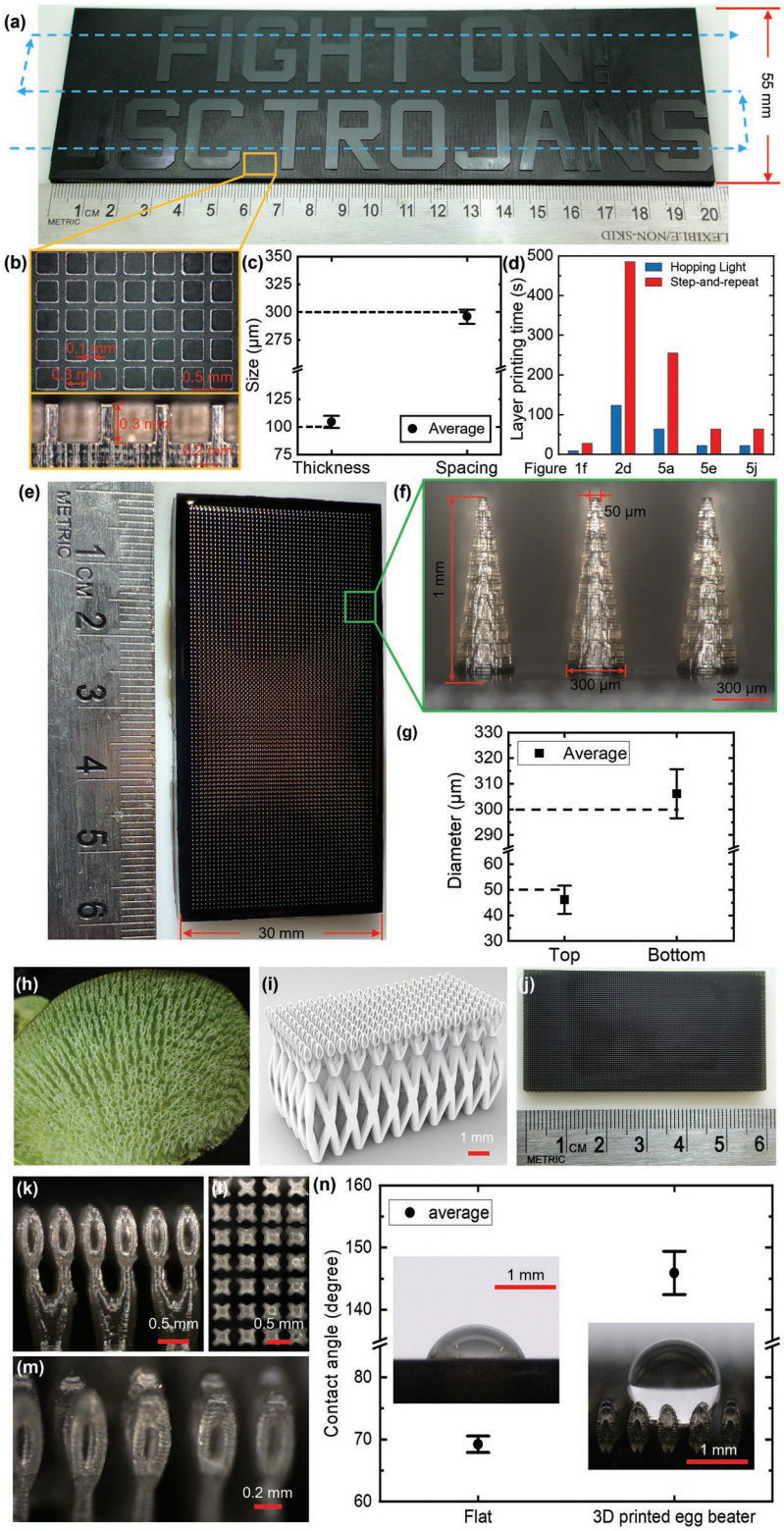

Figure 5. Test cases using the HL-VPP prototype. a) A large-area part with both microscale features and macroscale features. b) Microscope captured images of the printed microgrids (top and side views). c) Measurement results of cross-sectional dimensions of the printed microgrids. d) Comparison of the fabrication time of HL-VPP and the step-and-repeat methods. e) 3D-printed micropillar arrays (top view). f) Side view of 3D-printed micropillars. g) Measured diameters of the printed micropillars' top and bottom layers. h) Morphology of Salvinia molesta's leaf. The upper side of the leaf surface is densely covered with eggbeater hairs. Reproduced with permission.[50] Copyright 2008, Mic Julien, Commonwealth Scientific and Industrial Research Organization, Bugwood.org. i) Model of biomimetic eggbeater structures inspired by Salvinia molesta. j–m) 3D-printed eggbeater arrays. Top view: (j) and (l). Side view: (k). Isotropic view: (m). n) Contact angle test results and pictures for 3D-printed surfaces with and without eggbeater structures.

microscale VPP but reducing the printing time by 66% (Figure 5d).

Salvinia molesta's leaf possesses a unique superhydrophobic property because of the eggbeater-like hairs (Figure 5h).[50] To mimic this interesting structure-related function, we designed the microscale artificial hairs with eggbeater heads inspired by Salvinia molesta leaf (Figure 5i). The biomimetic surfaces fabricated by HL-VPP are shown in Figure 5j–m. The time saving for each layer fabrication is 66% (Figure 5d). Compared to our previous work (part size is ≈3 mm),[19] the proposed HL-VPP can fabricate hydrophobic structures over an arbitrarily large flat surface which enables applications such as bioinspired microfluidic devices in the future. We focused on hydrophobicity verification by measuring water contact angles in this test case. Figure 5n and Table S6 (Supporting Information) show that the 3D-printed eggbeater structure behaves like a nearly super-hydrophobic surface with a contact angle of 146°, even though the resin material shows a hydrophilic property with a contact angle of 69° on a flat surface. All the demonstrated test cases verify the HL-VPP method can reliably print multiscale parts accurately to realize small features' functionality. The process parameters are summarized in Table S7 (Supporting Information).

3. Conclusion

This work presents a novel multiscale AM process to fabricate 3D macroscale objects with microscale features. A significant contribution of our work is to propose the hopping light concept to optimize fabrication speed, resolution, and printing size simultaneously with dramatically reduced demand on the projector's refresh rate. By utilizing a galvo mirror to compensate for the image motion caused by the continuous linear moving of a projection system, our method can successfully correct the motion blur and enable a highly efficient VPP printing using a low image refresh rate. We provided a detailed methodology for constructing the motion synchronization and calibrating the process parameters using computer vision algorithms. Also, we derived the critical image marching distance to ensure the fabrication resolution will not be affected by the defocus of the tilted image. We demonstrated the fabrication of 3D objects with macroscale sizes of 200 mm and microscale feature size of 50 µm using a 10 µm pixel size, 13.5 mm s^{-1} scanning speed, and 10 Hz refresh rate. The theoretical and experimental results have verified our proposed method.

The HL-VPP's performance and functionality could be further enhanced and expanded in our future work. For instance, i) the printing area could be easily extended by using *XY* linear stages with larger travel ranges; ii) with a higher image refresh rate (e.g., 120 Hz, vs 10 Hz currently used), our HL-VPP process's printing speed can be further scaled up. The image refresh rate is not only determined by the projector hardware but also by the computer graphics and control system and the photocurable resin. Therefore, more efficient control software and faster curing resin need to be developed to match the 10 × higher refresh rate; iii) a specifically designed DLP light engine for HL-VPP instead of a refitted one can be integrated to increase the printing resolution (e.g., 2 µm per pixel); iv) for bottom-up VPP, increased separation force for a larger build area could be a significant issue. The vibration-assisted separation mechanism[14,51] or different release film can be utilized to avoid print failure due to excess separation force; v) novel applications that require macroscale area with microscale textures need to be identified for HL-VPP.[52,53] We envision this process could open a new avenue for large-area, fast-speed, and high-resolution VPP fabrication and future applications.

4. Experimental Section

HL-VPP Hardware: The HL-VPP prototype consists of two additional motorized linear stages—*XY* stages (404XR Series, Parker Hannifin; and PRO165SL, Aerotech) and a one-axis galvo mirror (S9650, Sunny Technology), compared with the traditional static bottom-up-projection-based VPP. Unlike other methods requiring customized components such as f-theta lens[34] or extremely-high-refresh-rate projector and graphics controller,[39–41] the setup was built up using off-the-shelf components only. The 405 nm UV DLP projector used in the prototype is from a commercial 3D printer (SprintRay Pro S, SprintRay, Los Angeles, CA). The projection system was modified by adding a lens to shrink the mask image size. After being reflected by the large galvo mirror, the mask image focus on a tank surface containing liquid resin. The large galvo mirror was designed to reflect a light beam with a diameter of 40 mm, which was sufficient for the purpose. The *Z*-axis (404XR Series, Parker Hannifin) holds an aluminum build platform, which carries the printing platform.

Software for HL-VPP: The CAD models of the test cases were designed in SolidWorks and then converted into STL files. An in-house built slicing software read the STL files and generated a set of layer mask images based on build area, resolution, and layer thickness. Then a C++ program split the sliced layer mask images into smaller ones based on single projection area size and generated corresponding G-codes for a given image marching distance and resin curing time.

An in-house developed control software read the mask images and G-codes and executed the printing jobs, including sending command and image data sequences to the motion controllers and the DLP projector. The control software in a personal computer (PC) was developed using Visual Studio and C++. The microcontroller (KFLOP & Kanolog, Dynomotion) received commands from the PC and synchronized the linear stage motion with the galvo mirror rotation by controlling the stepper motor driver (KStep, Dynomotion) and galvo mirror driver (SD-1000, Sunny Technology).

The prototype calibration system installed a handheld digital microscope (Plugable 250X Digital USB Microscope, Pluggable). The computer vision toolbox from MATLAB to assist in calibration was also leveraged. The corresponding algorithm is given in Table S2 (Supporting Information).

HL-VPP Fabrication and Characterization of Printing Results: Three types of resins (Anycubic clear, Anycubic; EnvisionTEC SI500, Perfactory; and Hard Tough Resin, eSun) were used in this work. The layer thickness was set to 80% of the curing depth, given the exposure time (namely, the projector's linear moving speed). The parameter setting can ensure good bonding between adjacent layers and surface quality. To ensure good adhesion between the fabricated part and the build platform, several adhesive layers for any print job with a longer exposure time (namely, slower projector scanning speed) were first printed. The printing parameters for all the test cases are listed in Table S7 (Supporting Information).

The fabricated parts were rinsed in pure 99% isopropanol twice after printing. The prints were then dried by an air pressure gun or just air-dried in the room environment for parts with delicate features. All the operations were conducted under low-light conditions. Precision measurement equipment (Sol 161, Micro-Vu) was used to measure the printed parts and capture the images. Twenty consecutive microgrids and micropillars were sampled and measured to evaluate the fabrication

accuracy. The measurement results are summarized in Tables S3 and S5 (Supporting Information). To quantify the hydrophobic property of the printed eggbeater structure, the water contact angle was measured and compared it with a flat surface. The experiments were repeated ten times. The corresponding results are summarized in Table S6 (Supporting Information) .

Supporting Information

Supporting Information is available from the Wiley Online Library or from the author.

Acknowledgements

Y.X. and H.M. contributed equally to this work. The authors acknowledge the support from National Science Foundation (NSF) (Grant Nos. CMMI 1151191, 1335476, and 1812675).

Conflict of Interest

Y.C. and H.M. are holders of a provisional U.S. patent related to this work (filed in May 2022). The authors declare no other competing interests.

Data Availability Statement

The data that support the findings of this study are available in the supplementary material of this article.

Keywords

additive manufacturing, computer vision, hopping light, multiscale, vat photopolymerization

Received: September 19, 2022
Revised: November 21, 2022
Published online: December 21, 2022

[1] C. W. Hull, US patent no 4,575,300, **1986**.
[2] J. C. Najmon, S. Raeisi, A. Tovar, in *Additive Manufacturing for the Aerospace Industry* (Eds: F. Froes, R. Boyer), Elsevier Inc., Amsterdam **2019**, pp. 7–31.
[3] Y. Yang, S. Li, H. Xu, Y. Xu, Y. Chen, *J. Manuf. Process.* **2022**, *74*, 88.
[4] L. Andjela, V. M. Abdurahmanovich, S. N. Vladimirovna, G. I. Mikhailovna, D. D. Yurievich, M. Y. Alekseevna, *Dent. Mater.* **2022**, *38*, e284.
[5] M. Ustun, S. R. Dabbagh, I. S. Ilci, T. Bagci-onder, S. Tasoglu, *Micromachines* **2021**, *12*, 490.
[6] U. Detamornrat, E. McAlister, A. R. J. Hutton, E. Larrañeta, R. F. Donnelly, *Small* **2022**, *18*, 2106392.
[7] L. Jiang, G. Lu, Y. Yang, Y. Xu, F. Qi, J. Li, B. Zhu, Y. Chen, *Adv. Mater.* **2021**, *33*, 2104251.
[8] M. Vehse, H. Seitz, *Int. J. Precis. Eng. Manuf.* **2014**, *15*, 2161.
[9] J.-H. Sim, E.-D. Lee, H.-J. Kweon, *Int. J. Precis. Eng. Manuf.* **2007**, *8*, 50.
[10] J. Stampfl, S. Baudis, C. Heller, R. Liska, A. Neumeister, R. Kling, A. Ostendorf, M. Spitzbart, *J. Micromech. Microeng.* **2008**, *18*, 125014.
[11] Y. Pan, C. Zhou, Y. Chen, *J. Manuf. Sci. Eng. Trans.* **2012**, *134*, 051011.
[12] J. R. Tumbleston, D. Shirvanyants, N. Ermoshkin, R. Janusziewicz, A. R. Johnson, D. Kelly, K. Chen, R. Pinschmidt, J. P. Rolland, A. Ermoshkin, E. T. Samulski, J. M. DeSimone, *Science* **2015**, *347*, 1349.
[13] D. A. Walker, J. L. Hedrick, C. A. Mirkin, *Science* **2019**, *366*, 360.
[14] Y. Xu, Y. Zhu, Y. Sun, J. Jin, Y. Chen, *J. Manuf. Sci. Eng. Trans.* **2021**, *143*, 051008.
[15] C. Sun, N. Fang, D. M. Wu, X. Zhang, *Sens. Actuators, A* **2005**, *121*, 113.
[16] H. Lee, N. X. Fang, *J. Vis. Exp.* **2012**, http://www.jove.com/video/4457.
[17] H. Gong, B. P. Bickham, A. T. Woolley, G. P. Nordin, *Lab Chip* **2017**, *17*, 2899.
[18] Y. Xu, F. Qi, H. Mao, S. Li, Y. Zhu, J. Gong, L. Wang, N. Malmstadt, Y. Chen, *Nat. Commun.* **2022**, *13*, 918.
[19] Y. Yang, X. Li, X. Zheng, Z. Chen, Q. Zhou, Y. Chen, *Adv. Mater.* **2018**, *30*, 1704912.
[20] H. Popper, *Pathology of Lung Disease*, Springer, Berlin **2017**.
[21] B. Maury, D. Salort, C. Vannier, *Networks Heterog. Media* **2009**, *4*, 469.
[22] M. Regehly, Y. Garmshausen, M. Reuter, N. F. König, E. Israel, D. P. Kelly, C. Y. Chou, K. Koch, B. Asfari, S. Hecht, *Nature* **2020**, *588*, 620.
[23] B. E. Kelly, I. Bhattacharya, H. Heidari, M. Shusteff, C. M. Spadaccini, H. K. Taylor, *Science* **2019**, *363*, 1075.
[24] P. N. Bernal, P. Delrot, D. Loterie, Y. Li, J. Malda, C. Moser, R. Levato, *Adv. Mater.* **2019**, *31*, 1904209.
[25] J. T. Toombs, M. Luitz, C. C. Cook, S. Jenne, C. C. Li, B. E. Rapp, F. Kotz-Helmer, H. K. Taylor, *Science* **2022**, *376*, 308.
[26] B. Busetti, B. Steyrer, B. Lutzer, R. Reiter, J. Stampfl, *Addit. Manuf.* **2018**, *21*, 413.
[27] W. Jia, Y.-S. Leung, H. Mao, H. Xu, C. Zhou, Y. Chen, *J. Manuf. Sci. Eng.* **2022**, *144*, 031003.
[28] H. Mao, Y. S. Leung, Y. Li, P. Hu, W. Wu, Y. Chen, *J. Micro Nano-Manuf.* **2017**, *5*, 040905.
[29] C. Yi, L. Dichen, W. Jing, *Rapid Prototyping J.* **2013**, *19*, 100.
[30] C. Zhou, Y. Chen, *J. Manuf. Processes* **2012**, *14*, 107.
[31] C. Zhou, H. Xu, Y. Chen, *Adv. Intell. Syst.* **2021**, *3*, 2100079.
[32] M. P. Lee, G. J. T. Cooper, T. Hinkley, G. M. Gibson, M. J. Padgett, L. Cronin, *Sci. Rep.* **2015**, *5*, 9875.
[33] R. Yi, C. Wu, Y. J. Liu, Y. He, C. C. L. Wang, *IEEE Trans. Autom. Sci. Eng.* **2018**, *15*, 1193.
[34] X. Zheng, W. Smith, J. Jackson, B. Moran, H. Cui, D. Chen, J. Ye, N. Fang, N. Rodriguez, T. Weisgraber, C. M. Spadaccini, *Nat. Mater.* **2016**, *15*, 1100.
[35] M. M. Emami, F. Barazandeh, F. Yaghmaie, *Sens. Actuators, A* **2014**, *218*, 116.
[36] M. M. Emami, F. Barazandeh, F. Yaghmaie, *J. Mater. Process. Technol.* **2015**, *219*, 17.
[37] V. Meenakshisundaram, L. D. Sturm, C. B. Williams, *J. Mater. Process. Technol.* **2020**, *279*, 116546.
[38] R. He, J. Landowne, J. Currie, J. Amoah, W. Shi, D. Yunus, Y. Liu, *Int. J. Adv. Manuf. Technol.* **2019**, *105*, 4147.
[39] K. Kambly, Characterization of Curing Kinetics and Polymerization Shrinkage in Ceramic-Loaded Photocurable Resins For Large Area Maskless Photopolymerization (Lamp), Georgia Institute of Technology, **2009**, https://smartech.gatech.edu/handle/1853/31740 (accessed: May 2022).
[40] A. Rudraraju, S. Das, in *20th Annu. Int. Solid Free.Fabr. Symp. SFF 2009*, University of Texas, Austin **2009**, pp. 299–307.
[41] Prodways, Prodways Movinglight® Technology, https://www.prodways.com/en/prodways-movinglight-technology/ (accessed: August 2022).

[42] I. Zubkov, Human lungs. Respiratory system. Healthy lungs. Light in the form of a tree. Black and white drawing on a chalkboard, https://www.dreamstime.com/human-lungs-respiratory-system-healthy-lungs-light-form-tree-black-white-drawing-chalkboard-human-lungs-image104933903 (accessed: August 2022).
[43] Paul Moews, Two Fish Plaques, https://www.thingiverse.com/thing:72403 (accessed: August 2022).
[44] L. Larmore, *Introduction to Photographic Principles*, Dover Publications, Inc., New York **1965**.
[45] imv, Tiger vector stock illustration, https://www.istockphoto.com/vector/tiger-vector-gm165626237-9369455 (accessed: August 2022).
[46] H. Bay, A. Ess, T. Tuytelaars, L. Van Gool, *Comput. Vision Image Understanding* **2008**, *110*, 346.
[47] C. Hao, Y. Liu, X. Chen, J. Li, M. Zhang, Y. Zhao, Z. Wang, *Small* **2016**, *12*, 1825.
[48] X. Li, Y. Yang, L. Liu, Y. Chen, M. Chu, H. Sun, W. Shan, Y. Chen, *Adv. Mater. Interfaces* **2020**, *7*, 1901752.
[49] Y. Zuo, L. Zheng, C. Zhao, H. Liu, *Small* **2020**, *16*, 1903849.
[50] M. Julien, giant salvinia, https://www.forestryimages.org/browse/detail.cfm?imgnum=0002106, (accessed: August 2022).
[51] J. Jin, J. Yang, H. Mao, Y. Chen, *J. Manuf. Process.* **2018**, *34*, 793.
[52] X. Li, T. Baldacchini, Y. Chen, *J. Micro Nano-Manuf.* **2021**, *9*, 041005.
[53] X. Liu, H. Gu, H. Ding, X. Du, Z. He, L. Sun, J. Liao, P. Xiao, Z. Gu, *Small* **2019**, *15*, 1902360.